ORIGINAL ARTICLE

Structural design principle and experimental study of the mixed-frequency vibration tool holder

Fei Su[1,2] · Guangtao Liu[1,2] · Ziheng Zeng[1,2] · Minhao Jiang[1,2]

Abstract

Fiber-reinforced polymer and metal-laminated structures are widely used in aerospace and military fields because of their excellent mechanical and physical properties. However, the materials are prone to processing defects such as burring and furry during processing. According to the mechanism of vibration cutting, the mixed-frequency vibration tool holder (MFVT) with low frequency and ultrasonic-combined vibration is designed and manufactured in this paper. The low-frequency vibration module (LFVM) and the ultrasonic vibration module (UVM) of the tool holder are designed theoretically and studied experimentally. The working performance and stability of the MFVT are tested and analyzed. The results show that the combination of ultrasonic vibration and low-frequency vibration of the tool holder can meet the requirements of design and tool holder. Among them, the exciting surface has the greatest influence on the motion curve of the LFVM. The amplitude of low-frequency vibration decreases with the increase of tool holder speed. When the UVM is running continuously, the temperature rise tends to be balanced. The amplitude and resonant frequency of ultrasonic vibration will decrease with the increase of operating temperature. The heat generated at the end of the cutter chuck accounts for the total heat generated by the horn 98.7% of the amount, the stable temperature reached 231℃.

Keywords Tool holder · Low-frequency vibration · Ultrasonic vibration · Fiber-reinforced polymer

1 Introduction

Fiber-reinforced polymer and metal laminated structures are widely applied in fields such as aerospace, aviation, and military, due to the excellent material properties [1–3]. In practical applications, it is often necessary to process fiber-reinforced polymer and metal-laminated structures to meet the requirements of use. However, defects such as delamination and tearing are easy to occur in the fiber-reinforced polymer and metal-laminated structure in processing [4]. Therefore, achieving precise, efficient, and low-defect processing of fiber-reinforced polymer and metal-laminated structures has become a crucial research direction for scholars.

Research indicates that vibration-assisted processing has many advantages compared to traditional machining, including reducing cutting forces, decreasing delamination defects, and improving machining surface quality. In the processing of fiber-reinforced composite metal-laminated structures, many scholars have carried out a lot of research on vibration-assisted processing technology. The types of vibration-assisted processing mainly include the low-frequency vibration-assisted processing and the ultrasonic vibration–assisted processing. Lee et al. [5] pointed out that in single-hole drilling, anti-EDM processing, and multi-hole processing, low-frequency vibration is helpful to improve processing speed. Lukas et al. [6] pointed out that low-feed speed can obtain better inlet quality and high amplitude feed ratio can obtain better outlet quality when low frequency vibration drilling CFRP/Al laminated structure. Oliver et al. [7] summarized the tool wear of CFRP/Ti6Al4V-laminated structure was drilled with low-frequency vibration. It was found that the application of low-frequency vibration significantly reduced the tool wear and cutting temperature. Sadek

✉ Fei Su
sfeihe@163.com

1   Hunan Provincial Key Laboratory of High Efficiency and Precision Machining of Difficult-to-Cut Material, Hunan University of Science and Technology, Xiangtan 411201, China

2   Intelligent Manufacturing Institute of HNUST, Hunan University of Science and Technology, Xiangtan 411201, China

et al. [8] carried out drilling tests on CFRP using the method of low-frequency vibration drilling. The results show that the drilling temperature and axial force of drilling processing during low-frequency vibration drilling are reduced by 50% and 40% compared with ordinary drilling. Lu et al. [9] analyzed the relevant characteristics of ultrasound-assisted processing and established an axial force model. It is pointed out that compared with traditional processing, the ultrasonic-assisted drilling force of CFRP is reduced by 22.8~32.7%. Xu et al. [10] used longitudinal torsion ultrasonic vibration milling to processing AFRP, and the results showed that the ultrasonic-assisted processing burr had outstanding improvement and enhancement effect, and the enhancement range was between 23 and 38%. Cong et al. [11, 12] concluded that rotary ultrasonic vibration drilling can reduce cutting force and torque. Ultrasonic vibration significantly decreases processing defects at the inlet of CFRP and the outlet of the titanium alloy. Zhang et al. [13] pointed out that the low-frequency vibration has better chip breaking effect on the processing of titanium alloy and can reduce the drilling temperature to the greatest extent. Ultrasonic vibration effectively reduces the drilling axial force. High- and low-frequency composite vibration drilling has addressed the issue of coordinating various material processing techniques for CFRP/titanium alloy–laminated structures. In conclusion, ultrasonic vibration–assisted processing is advantageous for the removal of brittle materials. Low-frequency vibration is beneficial for chip formation in ductile materials and reducing cutting temperatures. The combination of both can effectively reduce machining defects and improve processing quality.

Because vibration-assisted processing has many advantages, many scholars have carried out a lot of research on the design of vibration-assisted processing equipment. Ma et al. [14] developed a mechanical low-frequency drilling device using a swinging guide rod mechanism. The device can withstand large loads during operation. The amplitude and frequency are easily adjusted. Wu et al. [15] studied a mechanical axial vibration worktable. The worktable achieves axial vibration through a conical roller, cam structure, and spring. Laporte et al. [16] designed a low-frequency vibration-assisted processing device using spring pile as elastic recovery mechanism. Jiao et al. [17] utilized a novel annular flexible hinge as an elastic recovery mechanism and developed a low-frequency vibration-assisted drilling device. Liu et al. [18] designed a tool holder with low-frequency mechanical axial vibration. The tool holder uses the rotating motion of the spindle of the machine tool as the power input to drive the rotation of the sinusoidal surface and realize the amplitude output. Low-frequency vibration-assisted processing devices mainly achieve low-frequency vibration through methods such as electromagnetic, hydraulic, and mechanical means [19]. Due to its simple structure

and stronger stability in output motion curves, the mechanical low-frequency vibration devices are widely used in low-frequency vibration-assisted machining.

Scholars have also conducted numerous studies on ultrasonic-assisted machining devices. Xu et al. [20] proposed an ultrasonic-assisted milling platform for workpiece vibration. The experimental results show that the designed device can effectively reduce cutting force and improve processing accuracy. Harkness et al. [21] employed two methods to achieve a longitudinal-torsional–coupled vibration. One method is by machining spiral grooves on the side of the horn, transforming longitudinal vibration into longitudinal-torsional vibration. The other method is longitudinal-torsional coupling. Al-Budairi et al. [22] transformed the longitudinal vibration generated in the transducer into a longitudinal-torsional vibration response by modifying the geometric parameters of the waveguide. The method of altering the system frequency and torsional deflection was proposed. Tsujino et al. [23] used the method of creating oblique grooves on the surface near the nodes of a one-dimensional longitudinal vibration transducer to achieve longitudinal-torsional resonance at the same frequency. Nath et al. [24] pasted PZT on the vertical plane of the stepped amplitude lever, achieving accurate control of the output of double-bending ultrasonic elliptical vibration. Kim et al. [25] arranged two groups of piezoelectric ceramic pieces in vertical and parallel ways respectively. Utilizing harmonic signals with a phase difference to excite two sets of piezoelectric ceramic elements achieves ultrasonic elliptical vibration. Currently, the design of ultrasonic processing devices is mainly divided into one-dimensional, two-dimensional, and three-dimensional. Two-dimensional longitudinal-torsional composite ultrasonic processing devices have gained favor among scholars due to the simple structure and excellent processing characteristics.

Based on the advantages of ultrasonic vibration–assisted machining and low-frequency vibration-assisted machining, scholars have designed processing devices that combine ultrasonic vibration and low-frequency vibration. Ishikawa et al. [26] designed a new drilling device that combined ultrasonic vibration of diamond core drilling with low-frequency vibration of the workpiece. They pointed out that the combination of ultrasonic and low-frequency vibration is one of the most effective methods for drilling hard and brittle materials. Meng et al. [27] proposed a high and low frequency combined vibration drilling device by adding a low-frequency vibration form along the drilling direction. Li et al. [28] developed an integrated high-low frequency composite vibration processing tool holder. The tool holder achieves the composite vibration of high frequency and axial low frequency. At present, the high-frequency and low-frequency composite vibration processing devices are mainly split type and integrated type. The split-type device

is difficult to operate in practice and difficult to ensure accuracy, so it is necessary to develop an integrated composite vibration device.

Currently, single ultrasonic or low-frequency processing devices have been widely applied. The technology is relatively mature. However, the research of ultrasonic- and low-frequency-combined vibration processing equipment is rare. The MFVT with low-frequency and ultrasonic compound vibration is proposed. The LFVM and the UVM of the tool holder are designed theoretically. And the tool holder is studied experimentally. The vibration performance of the tool holder after processing is tested. Then, the position accuracy of the LFVM is deeply analyzed. The influence of position error and input speed on low-frequency vibration curves is analyzed by dynamic simulation. The vibration self-heating phenomenon of the UVM is simulated and verified by experiment. The effects of the ultrasonic vibrator temperature on amplitude and resonant frequency are analyzed by experiments and calculations.

2 Design concepts of MFVT

The mixed-frequency vibration combines high-frequency vibration with axial low-frequency vibration. Mixed-frequency devices can be divided into two types. The first is the integrated composite vibration processing device. The second is the modular composite vibration device. In each module, only one mode of vibration can be realized. Among them, the realization of the second type of device is more complicated, and the actual processing operation is difficult. Therefore, the integrated compound processing device is used to design the MFVT. As shown in Fig. 1, the design of the MFVT can be divided into two parts: the LFVM and the UVM.

From the motion trajectory equation of ultrasonic vibration and low-frequency vibration, the motion trajectory equation of mixing vibration can be obtained, as shown in Eq. (1).

$$
\begin{cases}
x(t) = V_f t + R_T sin(2\pi nt/60 + \omega) \\
\quad y(t) = R_T cos(2\pi nt/60 + \omega) \\
z(t) = A_D sin(f_D \times 2\pi nt/60) + A_H sin(2\pi f_H t) \\
\quad \omega = A_T cos(2\pi f_H + \varphi)
\end{cases}
\tag{1}
$$

Among them, the milling feed speed is represented by V_f, the milling tool radius is represented by R_T, the spindle speed of the machine tool is represented by n, the ultrasonic longitudinal amplitude is represented by A_H, the ultrasonic torsion amplitude is represented by A_N, the low-frequency amplitude is represented by A_L, the ultrasonic vibration frequency is represented by f_H, the low-frequency vibration frequency is represented by f_D, and the Angle of torsion of ultrasonic vibration is ω.

The LFVM includes a toroidal exciting surface, ball cage, spline coupling, and return spring. The excitation ring is a circular sinusoidal surface plate. One side is a plane connected with the spline coupling. The other side is a sinusoidal exciting surface to provide excitation for the realization of low-frequency vibration. The ball cage is the fixed part of the LFVM. The ball cage comprises an upper cover plate and a cage, and the steel ball is embedded between the two. The spline coupling is the transmission mechanism of the low-frequency vibration module and is fixed and connected with the toroidal exciting surface. Two return springs are placed on each side of the end of the spline coupling to provide the preload force for the contact between the ball and the excitation surface.

The UVM includes the ultrasonic power supply, the conductive slip ring, and the ultrasonic vibrator. The role of the ultrasonic power supply is to provide high-frequency

Fig. 1 Structural design and spatial motion trajectory of the MFVT
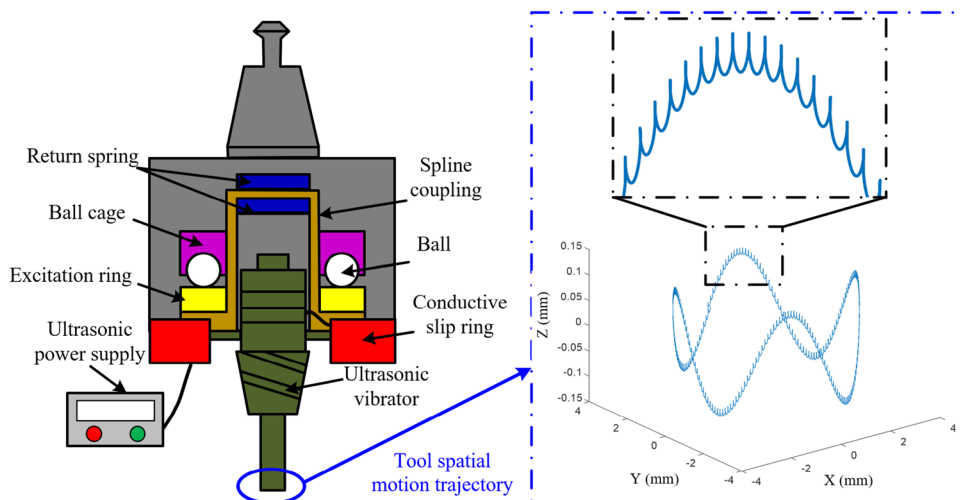
AC electrical signals matching the ultrasonic transducer. The alternating current signal can supply the excitation for the ultrasonic vibrator to generate vibration. The excitation current is transmitted through the conductive slip ring. The ultrasonic vibrator comprises a transducer and a horn. The high-frequency alternating current electrical signal is converted into high-frequency mechanical vibration by the piezoelectric effect of the piezoelectric ceramic plate. The end of the horn holds the tool and causes the tool to vibrate ultrasonic.

3 Design principles and modeling of the MFVT

3.1 Design principle of LFVM

The MFVT adopts the CAM structure to realize low-frequency vibration, so the realization of low-frequency vibration is directly related to the surface of excited vibration. Therefore, it is necessary to choose a reasonable motion law and design the corresponding exciting surface. When selecting the motion law of low-frequency vibration, v_{max} (the maximum velocity), a_{max} (the maximum acceleration), and j_{max} (the acceleration change rate) of the motion curve should be considered. These parameters affect the performance of the LFVM in different aspects. The smaller maximum velocity reduces mechanical wear between contact parts. The magnitude of the maximum acceleration directly affects the magnitude of the reciprocating inertial force of the LFVM during operation. The smaller rate of acceleration change can reduce the flexibility impact between components. The motion performance of sinusoidal acceleration motion is balanced and chip breaking can be realized during processing. The characteristics of sinusoidal acceleration motion are suitable for the working conditions of the tool holder. Therefore, the sinusoidal acceleration motion curve is selected as the motion output curve of the LFVM.

The displacement output curve of sine acceleration motion can be expressed as a sine function as follows: $H = A_D \sin(2\pi f_D t)$. The excitation surface of the toroidal exciting surface is designed according to the motion track of low-frequency vibration. In the LFVM, the desired low-frequency vibration motion is realized by the contact transmission between the excitation surface and the ball surface. The excitation surface and the ball surface need to be designed to match each other to ensure good contact between the two parts. The matching design between components is beneficial to achieve accurate motion curve control. The principle of conjugate surfaces provides an efficient, accurate, and stable method for the design of the excitation surface. The principle of conjugate surface can improve motion control and reduce wear, thereby improving the performance

and reliability of mechanical systems. Therefore, according to the determined structural parameters and motion law requirements, the excitation surface is designed using the conjugate surface principle.

From the design concept of the excitation surface, it can be known that the designed excitation surface is tangent to the ball surface at any given moment. That is, the relative velocity Δv between the cam excitation surface and the ball surface is perpendicular to the normal vector n of the contact point. The meshing condition between the excitation surface and the ball surface is $\Delta v \cdot n = 0$. The meshing condition can be converted in differential geometry to as follows [30]:

$$(\overrightarrow{R_\delta}, \overrightarrow{R_l}, \overrightarrow{R_\theta}) = 0 \tag{2}$$

In the LFVM, the surface profile of the ball has been determined. The excitation surface is derived using the conjugate surface principle. As illustrated in Fig. 2, the $s(o\text{-}xyz)$ coordinate system is a fixed coordinate system, the z-axis coincides with the rotation center axis of the excitation surface, and the origin o is located at the center of the ball disk motion trajectory. The $s_1(o_1\text{-}x_1y_1z_1)$ coordinate system is a moving coordinate system and is fixedly connected to the excitation ring. The origin o_1 coincides with the origin o of the s coordinate system. As the excitation surface rotates around the z-axis of the s coordinate system. The angle of rotation is set to θ. The coordinate system $s_2(o_2\text{-}x_2y_2z_2)$ is also a moving coordinate system and is fixedly connected to the balls on the ball cage. Among them, the directions of each directional axis of the s_2 coordinate system are consistent with the s coordinate system. The origin o_2 reciprocates with the ball along the z-axis of the s coordinate system.

A certain contact point P is taken between the excitation surface and the ball, as presented in Fig. 2.

The coordinates of the contact point P in the s, s_1, s_2 coordinate systems are as follows:

$$
\begin{cases}
\vec{R}^{(2)} = \begin{pmatrix} r\sin\delta \\ l_0 + l \\ -r\cos\delta \end{pmatrix} \\
\vec{R} = \vec{R}^{(2)} + \begin{pmatrix} 0 \\ 0 \\ H \end{pmatrix} = \begin{pmatrix} r\sin\delta \\ l_0 + l \\ -r\cos\delta + H \end{pmatrix} \\
\vec{R}^{(1)} = E^{k\theta}\vec{R} = \begin{pmatrix} r\sin\delta\cos\theta - (l_0 + l)\sin\theta \\ r\sin\delta\sin\theta + (l_0 + l)\cos\theta \\ -r\cos\delta + H \end{pmatrix}
\end{cases} \tag{3}
$$

Among them, the right superscript is the coordinate system number, l_0 is the distance between the inner surface of the ball and the origin, l is the projection of the contact point P on the
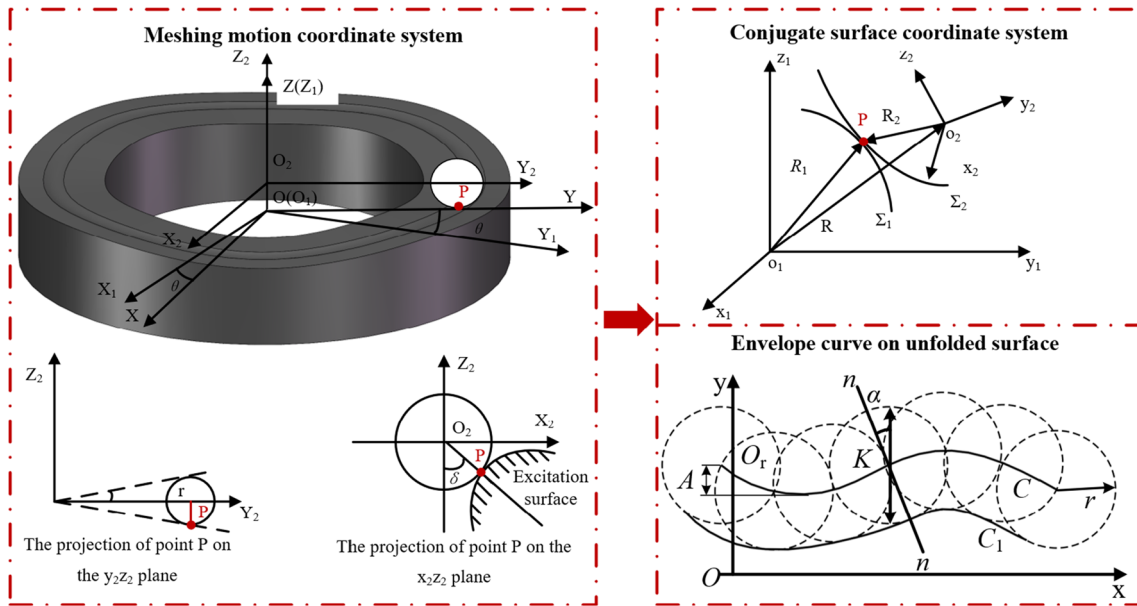
Fig. 2 Design of excitation surface of the LFVM

y-axis of the s_2 coordinate system, and δ is the contact angle between the ball and the excitation curved surface at the position radius of point P, $E^{k\theta}$ is the transformation matrix from the s coordinate system to the s_1 coordinate system, H is the low-frequency vibration displacement curve.

Calculate the partial derivative of point P in the s_1 coordinate system with respect to δ, l, and θ, as follows:

$$
\begin{cases}
\vec{R}_\delta^{(1)} = \begin{pmatrix} r\cos\delta\cos\theta \\ r\cos\delta\sin\theta \\ r\sin\delta \end{pmatrix} \\[2ex]
\vec{R}_l^{(1)} = \begin{pmatrix} -\sin\theta \\ \cos\theta \\ 0 \end{pmatrix} \\[2ex]
\vec{R}_\theta^{(1)} = \begin{pmatrix} -(l_0+l)\sin\theta - r\sin\theta\sin\delta \\ -(l_0+l)\cos\theta + r\cos\theta\sin\delta \\ H' \end{pmatrix}
\end{cases}
\tag{4}
$$

From the meshing conditions of the contact point P, the direction angle δ of the contact point P can be obtained. The equations of the convex profile surface of the excitation surface can be obtained by sorting out the equations as follows:

$$
\begin{cases}
\vec{R}_\theta^{(1)} = \begin{pmatrix} -(l_0+l)\sin\theta - r\sin\theta\sin\delta \\ -(l_0+l)\cos\theta + r\cos\theta\sin\delta \\ H' \end{pmatrix} \\[3ex]
\delta = \arctan\dfrac{H'}{l_0+l}
\end{cases}
\tag{5}
$$

In the LFVM, the balls contact and move relative to the excitation surface, and the pressure angle affects the movement of the mechanism. The smaller pressure angle can reduce the normal force at the contact point, thereby reducing wear and increasing the service life of the mechanism. The pressure angle in the LFVM is the angle between the contour curve of the excitation surface and the ball in the normal direction of the contact point, as shown in Fig. 2. The magnitude of the pressure angle depends on the design of the excitation surface profile and the geometry of the balls. The structural parameters of the excitation surface are determined by reasonably designing the pressure angle. The expression of pressure angle α_s is as follows [29]:

$$\begin{cases} \tan \alpha_s = \left| \dfrac{dy}{dx} \right| = \dfrac{1}{D} \dfrac{ds}{d\varphi} = \dfrac{nA}{D} |\sin(n\omega t)| \\ \alpha_s = \arctan[\dfrac{nA}{D} |\sin(n\omega t)|] \end{cases} \quad (6)$$

According to the expression formula of the pressure angle, the size of the pressure angle αs is only related to the base cylinder radius D of the excitation cam surface and the running time t of the low-frequency vibration module. In the design of the low-frequency vibration module, the movement law of the follower has been determined, that is, the t has been determined. Therefore, we only need to consider the influence of the base cylinder radius D of the excitation surface on the pressure angle. The larger the base cylinder radius D, the smaller the pressure angle α_s.

According to the profile equation and structural parameters of the excitation surface, the three-dimensional model of the excitation surface is established. Since the ball is in point contact with the excitation surface, it is easy to cause fatigue and wear of the contact point. The surface trajectory on the excitation surface is set according to the size of the ball, as shown in Fig. 3.

3.2 Dynamic theory and accuracy analysis modeling of LFVM

The LFVM is composed of multiple parts, and the theoretical rigid connection between the parts cannot be achieved in actual work. The frictional resistance between connected parts is not zero. The contact cannot be uniform. All parts are not absolutely rigid bodies and will undergo slight deformation during the operation of the LFVM. If all factors are taken into account to establish a dynamic model of the LFVM, the model will be complicated. In general, the complex dynamic models are not conducive to solution and interfere with the analysis of the dynamic characteristics

of the LFVM. To sum up, when establishing the dynamic model of the LFVM, some secondary factors that have a small impact on the dynamic characteristics (such as machining errors, friction between the ball and the excitation surface) are ignored. Each component of the LFVM is assumed to be a rigid body and all are rigidly connected.

As shown in Fig. 3, the dynamic model of the LFVM is established. The lower end surface of the excitation plate is used as the starting point of the displacement of the LFVM. At this time, the ball is located at the high point of the excitation surface. According to the Newton–Euler equation analysis, the dynamic balance equation of the LFVM can be obtained.

$$c\frac{dz}{dt} + k_1(z + l_0) + k_2(z + l_0) = F_n(t) + Mg + M\frac{d^2z}{dt^2} \quad (7)$$

In the formula, M is the overall weight of the excitation ring and the UVM, in kg; k_1, k_2 are the stiffness coefficients of the spring; c is the viscous damping coefficient of the spring; z is the lower end surface of the toroidal exciting surface. The output displacement of the starting point; l_0 is the initial preload of the spring.

For the simple harmonic motion of the LFVM as follows:

$$\begin{cases} z = A \sin(n\omega t) \\ \dfrac{dy}{dt} = An\omega \cos(n\omega t) \\ \dfrac{d^2y}{dt^2} = -An^2\omega^2 \sin(n\omega t) \\ F_n(t) = A(2k + N^2\omega^2 M) \sin(N\omega t) + 2cAn\omega \cos(n\omega t) + 2kl_0 - Mg \end{cases} \quad (8)$$

where ω is the angular velocity of the output shaft, rad/s.

When the excitation cam curved surface remains in contact with the ball, the pressure surface at the bottom of the ball concentrates the tangential reaction force generated by the driving torque. According to the torque balance, the dynamic equation of the LFVM can be obtained as follows:
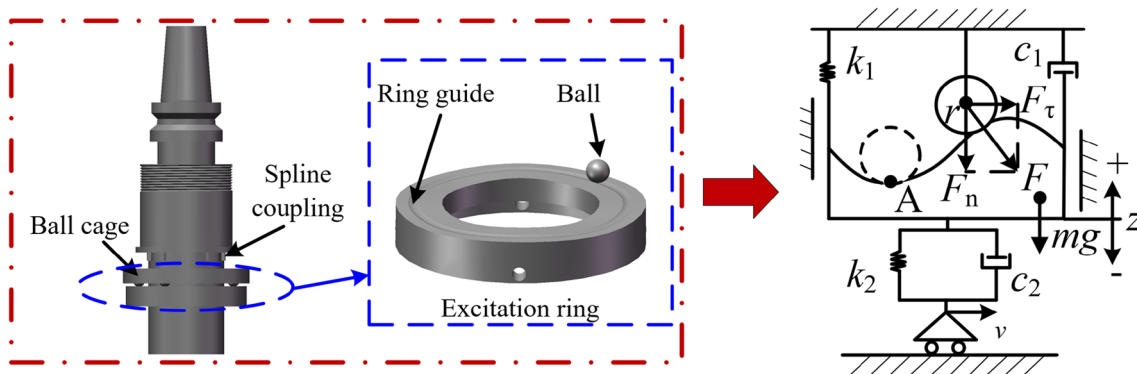

Fig. 3 Dynamic model of LFVM

$$\begin{cases} T = F_\tau D = F_n \times \tan \alpha_s \times D \\ T(t) = nA^2(k + n^2\omega^2 M)\sin^2(n\omega t) + \dfrac{cA^2n^2}{2}\sin(2n\omega t) + nA(kl_0 - Mg)\sin(n\omega t) \end{cases} \tag{9}$$

The LFVM is a force-closed vibration system. The return spring is to ensure that the excitation surface and the ball are always in contact during the operation of the mechanism. A reasonable selection of the stiffness and preload amount of the spring will help prevent deviations in the movement pattern of the mechanism. Excessive spring preload will increase the contact stress between the excitation cam surface and the balls.

According to the established dynamic equation, dimensionless quantities are introduced into the dynamic equation [30] as follows:

$$\begin{cases} F_0(t) = \dfrac{F_n(t)}{Ak} \\ \delta = \dfrac{n\omega}{\omega_n} \\ \xi = \dfrac{c}{m\omega\omega_n} \\ \Delta = \dfrac{2kl_0 - Mg}{Ak} \\ F_0(t) = \sqrt{\left(1+\delta^2\right)^2 + \delta^2\xi^2}\sin(n\omega t + \eta) + \Delta, \tan\eta = \dfrac{1+\delta^2}{\delta\xi} \end{cases} \tag{10}$$

where ω_n is the natural frequency of the undamped system and c is the damping factor.

The expression of the minimum contact force between the excitation surface and the ball is as follows:

$$\begin{cases} \dfrac{dF_0}{dt} = n\omega\sqrt{(1+\delta^2)^2 + \delta^2\xi^2}\cos(n\omega t + \eta) = 0 \\ (F_0)_{\min} = \Delta - \sqrt{(1+\delta^2)^2 + \delta^2\xi^2} \end{cases} \tag{11}$$

where $\cos(n\omega t + \eta) = 0$.

The critical conditions for the separation of the excitation surface and the ball are as follows:

$$\Delta = \sqrt{(1+\delta^2)^2 + \delta^2\xi^2} \tag{12}$$

In the design of the LFVM, the preload amount l_0 of the spring should be selected so that the value of Δ is greater than the critical condition.

The processing error of the MFVT and the matching clearance of the kinematic pair will cause errors in the motion curve output by the LFVM. In order to control the output error of the LFVM, the common original errors in the low-frequency vibration module are analyzed. Assuming that all the forces in the mechanism are parallel to the motion

plane of the MFVT, the influence of various original errors on the axial output curve of the mechanism can be obtained.

(1) Local position error caused by ball cage gap

$$\Delta r = \Delta r_1 + \Delta r_2 \tag{13}$$

The outer diameter tolerance of the ball is $\Delta r1$, and the gap between the ball and the ball cage is $\Delta r2$. Therefore, the local position error of the push rod caused by the gap between the ball and the ball cage is as follows:

$$\Delta h_r = \frac{\Delta r}{\cos\alpha} = \frac{\Delta r_1 + \Delta r_2}{\cos\alpha} \tag{14}$$

where α is the pressure angle of the ball center on the theoretical profile of the excitation surface.

(2) Local position error caused by excitation surface contour error

The radial size of the excitation surface is $R + \Delta R$, so the original radial error of the cam outline is the dimensional tolerance as follows:

$$\Delta h_R = \Delta R \tag{15}$$

(3) Local position error caused by spline coupling gap error

For the spline coupling to move within the guide path, there must be a gap between the two. Then, there is as follows:

$$\begin{cases} \Delta h_\lambda = h - h\cos\lambda \\ \lambda = \arctan\dfrac{D_{\max} - d_{\min}}{l} \end{cases} \tag{16}$$

The superposition of the above local position errors constitutes the original axial error of the LFVM.

$$\Delta h_\Sigma = \Delta h_r + \Delta h_R + \Delta h_\lambda \tag{17}$$

Based on the above theoretical error calculation model, the ideal dynamics simulation model of the LFVM and the original position error dynamics simulation model of the LFVM. The models are established to analyze the impact of the original position error on the low-frequency vibration motion curve.
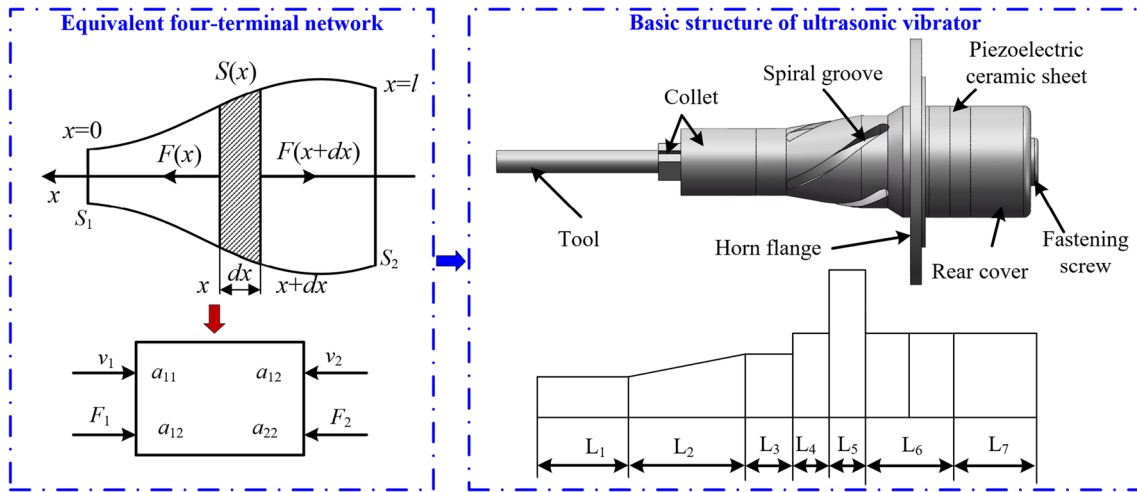
Fig. 4 Structural design of the ultrasonic vibrator

3.3 Design principle of UVM

Ultrasonic vibration is realized by the ultrasonic power supply, conductive slip ring, and ultrasonic vibrator. Among them, the ultrasonic vibrator is the most important component in the UVM. The ultrasonic vibrator will directly affect the ultrasonic vibration performance of the mixing tool holder. Therefore, the ultrasonic vibrator needs to be accurately designed.

It is assumed that the variable-section rod is composed of uniform and isotropic materials, and its mechanical loss is not considered. The plane longitudinal wave propagates along the axial direction of the variable-section rod, and the stress is evenly distributed on the cross-section of the variable-section rod. As displayed in Fig. 4, the central axis of the variable-section rod is the x-axis, and the left end surface of the variable-section rod is the origin of the x-axis. The longitudinal vibration wave equation of the variable-section rod can be obtained as follows:

$$\begin{cases} \dfrac{\partial^2 \varepsilon}{\partial x^2} + \dfrac{1}{S}\dfrac{\partial S}{\partial x}\dfrac{\partial \varepsilon}{\partial x} + k^2 \varepsilon = 0 \\ k = \sqrt{\omega^2/c^2} \\ c = \sqrt{\dfrac{E}{\rho}} \end{cases} \tag{18}$$

where $S = S(x)$ is the cross-sectional area function of the variable-section rod, $\varepsilon = \varepsilon(x)$ is the displacement function of the particle, ρ is the material density of the variable-section rod, k is the circular wave number, ω is the circular frequency, c is the propagation velocity of sound waves in the variable-section rod, and E is the Young's modulus of the cross-section rod material.

When the rod is a rod of equal cross-section, Eq. (24) can be simplified to as follows:

$$\frac{\partial^2 \varepsilon}{\partial x^2} + k^2 \varepsilon = 0 \tag{19}$$

According to the simple harmonic motion $v = j\omega\varepsilon$, the general solution of the Eq. (25) is as follows:

$$\begin{cases} v(x) = A\sin kx + B\cos kx \\ F(x) = \dfrac{E}{j\omega}\dfrac{\partial v}{\partial x} = -j\rho c(A\cos kx - B\sin kx) \end{cases} \tag{20}$$

where $F(x)$ is the stress distribution equation of the rod, A and B are undetermined coefficients, Z is the acoustic impedance characteristic of the rod, $Z = \rho c S$.

When the rod is a rod with a conical section, the general solution can be obtained from the Eq. (24):

$$\begin{cases} v(x) = \dfrac{1}{1-\alpha x}(A\sin kx + B\cos kx) \\ \alpha = \dfrac{D_1 - D_2}{D_1 l} \\ F(x) = \dfrac{E}{j\omega}\dfrac{\partial \varepsilon_1}{\partial x} = -\dfrac{j\rho c}{1-\alpha x}\left[A\left(\cos kx + \dfrac{\alpha \sin kx}{k(1-\alpha x)}\right) - B\left(\sin kx - \dfrac{\alpha \cos kx}{k(1-\alpha x)}\right)\right] \end{cases} \tag{21}$$

where D_1 and D_2 are the diameters of the big end and small end of the conical cross-section rod.

As shown in Fig. 4, according to the vibration velocity and stress continuity at the interface, the boundary condition on the right side of the ultrasonic vibrator node plane can be obtained as follows:

$$\begin{cases} v_{5L} = 0 \\ v_{6L} = v_{5R} \\ v_{6R} = v_{7L} \\ F_{5R} = F_{6L} \\ F_{6R} = F_{7L} \\ F_{7R} = 0 \end{cases} \tag{22}$$

The frequency equation on the right side of the node plane can be obtained as follows:

$$\frac{Z_7}{Z_6} \tan(k_6 l_6) \tan(k_7 l_7) + \frac{Z_6}{Z_5} \tan(k_5 l_5) \tan(k_6 l_6) + \frac{Z_7}{Z_5} \tan(k_5 l_5) \tan(k_7 l_7) = 1 \tag{23}$$

The horn on the left side of the node plane is a fourth-order horn, and it is easier to solve it using the four-terminal network method. Each section of the horn is equivalent to a mechanical four-terminal network. By using the continuity of stress and vibration velocity, the transmission matrix composed of each four-terminal network is multiplied successively. The overall transmission matrix of the composite horn is obtained. The frequency equation of the ultrasonic vibration system can be derived from the overall transmission matrix.

The basic structure and equivalent four-terminal network of a single-shaped rod are presented in Fig. 4. Among them, v_1 and v_2 are the vibration speeds of the input end and the output end; F_1 and F_2 are the elastic forces of the input end and the output end; a_{11}, a_{12}, a_{21}, and a_{22} are the four-terminal network parameters. The transmission characteristic equation of a single-section rod can be obtained as follows:

$$\begin{cases} \begin{bmatrix} v_2 \\ F_2 \end{bmatrix} = \begin{bmatrix} a_{11} & a_{12} \\ a_{21} & a_{22} \end{bmatrix} \begin{bmatrix} v_1 \\ F_1 \end{bmatrix} \\ A = \begin{bmatrix} a_{11} & a_{12} \\ a_{21} & a_{22} \end{bmatrix} \end{cases} \tag{24}$$

The four-terminal network parameters of the equal-section rod are as follows:

$$\begin{cases} a_{11} = a_{22} = \cos(kL_i) \\ a_{12} = \dfrac{-j \sin(kL_i)}{\rho c S_i} \\ a_{21} = -j\rho c S_i \sin(kL_i) \end{cases} \tag{25}$$

The four-terminal network parameters of the tapered cross-section rod are as follows:

$$\begin{cases} a_{11} = \dfrac{-(\alpha/k) \sin(kL_2) + \cos(kL_2)}{1 - \alpha L_2} \\ a_{12} = \dfrac{-j \sin(kL_2)}{\rho c S_2 (1 - \alpha L_2)} \\ a_{21} = \dfrac{\rho c S_2}{jk} \left\{ \left[k(1 - \alpha L_2) + \dfrac{\alpha^2}{k} \right] \sin(kL_2) - \alpha^2 L \cos(kL_2) \right\} \\ a_{22} = (1 - \alpha L_2) \cos(kL_2) + \dfrac{\alpha^2}{k} \sin(kL_2) \end{cases} \tag{26}$$

According to the transmission characteristics of the four-terminal network, the four-terminal network transmission matrix of the horn can be obtained. When the ultrasonic oscillator is unloaded, the frequency equation on the left side of the node plane is as follows:

$$\begin{cases} A = \begin{bmatrix} A_{11} & A_{12} \\ A_{21} & A_{22} \end{bmatrix} = \begin{bmatrix} a_{11}^4 & a_{12}^4 \\ a_{21}^4 & a_{22}^4 \end{bmatrix} \begin{bmatrix} a_{11}^3 & a_{12}^3 \\ a_{21}^3 & a_{22}^3 \end{bmatrix} \begin{bmatrix} a_{11}^2 & a_{12}^2 \\ a_{21}^2 & a_{22}^2 \end{bmatrix} \begin{bmatrix} a_{11}^1 & a_{12}^1 \\ a_{21}^1 & a_{22}^1 \end{bmatrix} \\ A_{22} = 0 \end{cases} \tag{27}$$

After completing the derivation of the frequency equation of the ultrasonic vibrator, the structural length of the ultrasonic vibrator can be designed according to requirements. In this article, the frequency of the ultrasonic vibrator is selected as 33 kHz, and the materials of the back cover and horn are selected as 45 steel. The detailed material parameters are shown in Table 2. Two annular PZT-8 piezoelectric ceramic sheets are selected, the size parameters are: outer diameter 30 mm, inner diameter 20 mm, and thickness 5 mm. The structural length of the ultrasonic vibrator is calculated through MATLAB, and the specific parameters are shown in Table 3.

3.4 Vibration self-heating simulation modeling of the UVM

When the UVM is working, the piezoelectric ceramic piece in the transducer is excited by the ultrasonic power source
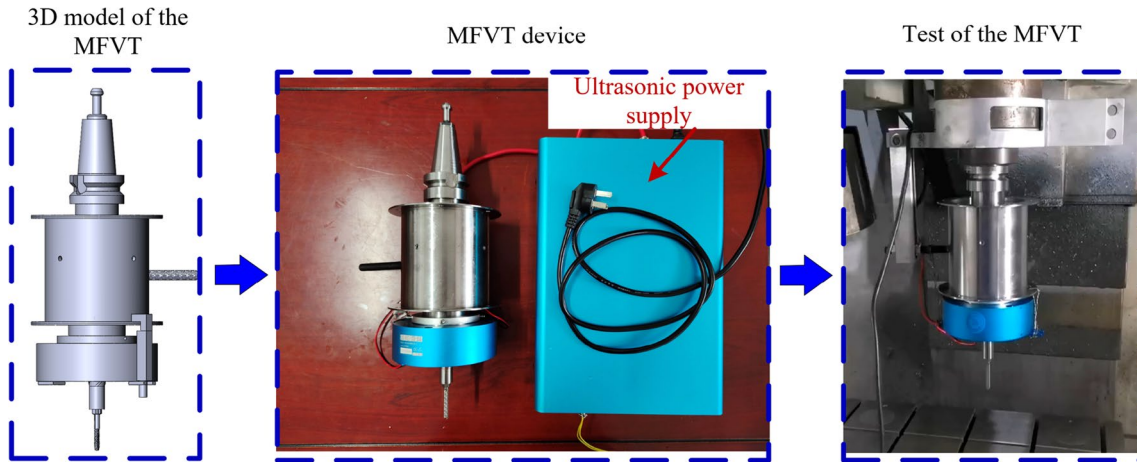
Fig. 5 The MVFT device and the 3D model of the MVFT

to generate high-frequency mechanical vibration. Due to the viscoelastic effect of the material, the vibration wave will produce mechanical losses and generate a large amount of heat during the propagation of the horn. As the main component of ultrasonic vibration, the piezoelectric ceramic sheet's inherent vibration frequency is greatly affected by temperature. As the temperature of the working environment increases, the energy conversion rate of the piezoelectric ceramic sheet will gradually decrease. When the extreme temperature is exceeded, the piezoelectric ceramic sheet will depolarize.

In order to study the heat energy generation mechanism of the UVM, the vibration self-heating simulation analysis of the horn was carried out through the finite element simulation software COMSOL. The vibration self-heating simulation combines the frequency domain analysis of the horn structure with the heat transfer simulation analysis to simulate the temperature rise of the UVM in the working process. According to the design principle of the horn, various parameters of the horn are obtained, and the overall three-dimensional simulation model of the horn is established, as shown in Fig. 4. Due to the complexity of the tool modeling, meshing is more difficult in the simulation analysis and has little impact on the simulation results. Therefore, the actual tool is replaced by a round bar of the same length and material in the analysis.

The coupling physical field analysis of heat transfer and structural mechanics in COMSOL was selected and the horn 3D simulation model was introduced. The whole model was meshed using the meshing component included with the simulation analysis software. In the material properties module, the material parameters of each structure are set respectively, as shown in Table 2.

In the solid mechanics module, the frequency domain type of the equation form is selected and the corresponding

Table 1 Design parameters of the excitation ring

Items	Value
Vibration amplitude	0.06 (mm)
Internal ring radius	145 (mm)
Ball radius	5 (mm)
Number of balls	4

Table 2 Main properties of the ultrasonic vibrator

Items		Value
45 steel	Thermal conductivity	48 W/(m·K)
	Density	7850 kg/m³
	Constant pressure heat capacity	460 J/(kg·K)
	Young's modulus	209 GPa
	Poisson's ratio	0.28
YG6X	Thermal conductivity	79.6 W/(m·K)
	Density	14600 kg/m³
	Constant pressure heat capacity	220 J/(kg·K)
	Young's modulus	640 GPa
	Poisson's ratio	0.22
PZT-8	Thermal conductivity	7 W/(m·K)
	Density	7500 kg/m³
	Constant pressure heat capacity	750 J/(kg·K)
	Young's modulus	60 GPa
	Poisson's ratio	0.31
65 Mn	Thermal conductivity	46.6 W/(m·K)
	Density	7800 kg/m³
	Constant pressure heat capacity	487 J/(kg·K)
	Young's modulus	170 GPa
	Poisson's ratio	0.29

Table 3 Size parameters the ultrasonic vibrator structural

Items	L2	L3	L4	L5	L6	L7
Value	16 mm	11 mm	7 mm	7 mm	20 mm	8 mm

Table 4 Thermophysical parameters of 45 steel

Items			Value
45 steel	Thermal expansion coefficient	20℃	11.6 (10^{-6}/℃)
		100℃	13.2 (10^{-6}/℃)
		200℃	14.8 (10^{-6}/℃)
	Young's modulus	20℃	209 GPa
		100℃	207 GPa
		200℃	202 GPa

frequency value is set. The vibration frequency of the horn is 33 kHz. The isotropic loss factor of each material and set the materials to linear elastic materials is added. Fixed constraints are added to the flange of the horn to simulate the actual working state of the horn. The displacement load is set at the rear end of the horn, that is, the excitation amplitude of the horn loaded by the transducer is simulated.

In the solid heat transfer analysis component, the rise in horn temperature is obtained from the heat transfer equation as follows:

$$\begin{cases} \rho C_p \dfrac{\partial T}{\partial t} - \nabla \cdot (k\nabla T) = Q_h \\ Q_h = \dfrac{1}{2}\omega\eta\text{Real}[\varepsilon : \text{Conj}(C : \varepsilon)] \end{cases} \quad (28)$$

where k is the thermal conductivity of the material, ρC_p is the volume-specific heat capacity, Q_h is the heat source, T is the average temperature in the time period of $2\pi/\omega$, η is the loss factor, ω is the angular excitation frequency, ε is the strain tensor, C is the elasticity tensor. According to the Dulong-Petit law, the volume-specific heat capacity has nothing to do with temperature.

The initial temperature of the horn and the external ambient temperature are both set to 293.15 K. Thermal insulation conditions are set at the rear end of the horn that bears the displacement load. The heat exchange mode between the horn and the external environment to convection heat exchange is set. The contact boundaries between the tool, chuck, and horn are set as internal boundaries. The convective exchange conditions between the remaining boundaries and the external environment are as follows:

$$n \cdot (-k\nabla T) = h(T - T_{\text{ext}}) \quad (29)$$

where h is the heat transfer coefficient, set to 20 W/(m²·K), T_{ext} is the external ambient temperature.

4 Experimental procedures

Through experimental research, the performance of the MFVT is analyzed, and the reliability of the LFVM and the UVM are analyzed. The performance of low-frequency vibration and ultrasonic vibration of the mixing tool holder was tested under different parameters. The changes in the self-heating temperature of the UVM and the influence of temperature on the vibration performance of the ultrasonic vibrator are analyzed, and the influence of the spindle velocity on the vibration performance of the LFVM is studied.

4.1 Experimental conditions

(1) Experimental subject

Experimental analysis was conducted on the MFVT, as shown in Fig. 5. The theoretical performance parameters are as follows: the vibration mode is longitudinal-torsional, the vibration frequency is 33 kHz, the axial amplitude is 5 μm, and the amplitude ratio of longitudinal vibration to torsional vibration is 1:1. The amplitude of low-frequency vibration is 60 μm.

According to the LFVM design theory, the design parameters of the excitation ring are selected, as shown in Table 1.

The material parameters of the ultrasonic vibrator are illustrated in Table 2.

The size parameters of each structure of the ultrasonic vibrator can be obtained from the frequency equation of the ultrasonic vibrator, as illustrated in Table 3.

The thermophysical parameters 45 steel are shown in Table 4.

(2) Experimental platform

The low-frequency vibration test was conducted on the VMC850LA CNC machine tool. The operating temperature of the ultrasonic vibrator is measured using the FLIR-SC325 infrared thermometer. The room temperature during the temperature measurement test is 20 °C. The amplitude was measured by KEYENCE LK-H020 laser displacement sensor. The impedance of ultrasonic vibrator was analyzed by the PV510A impedance analyzer. The MD-X2000A laser marking machine is used to mark the amplitude measuring plane on the cutting edge of the fish scale–milling tool.
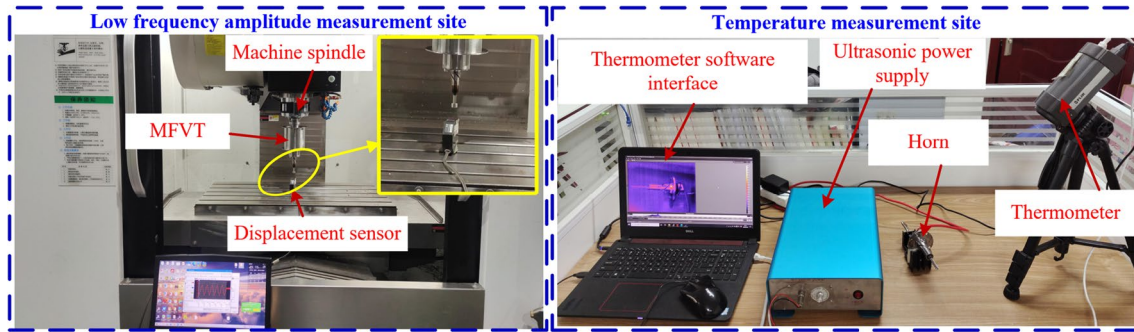
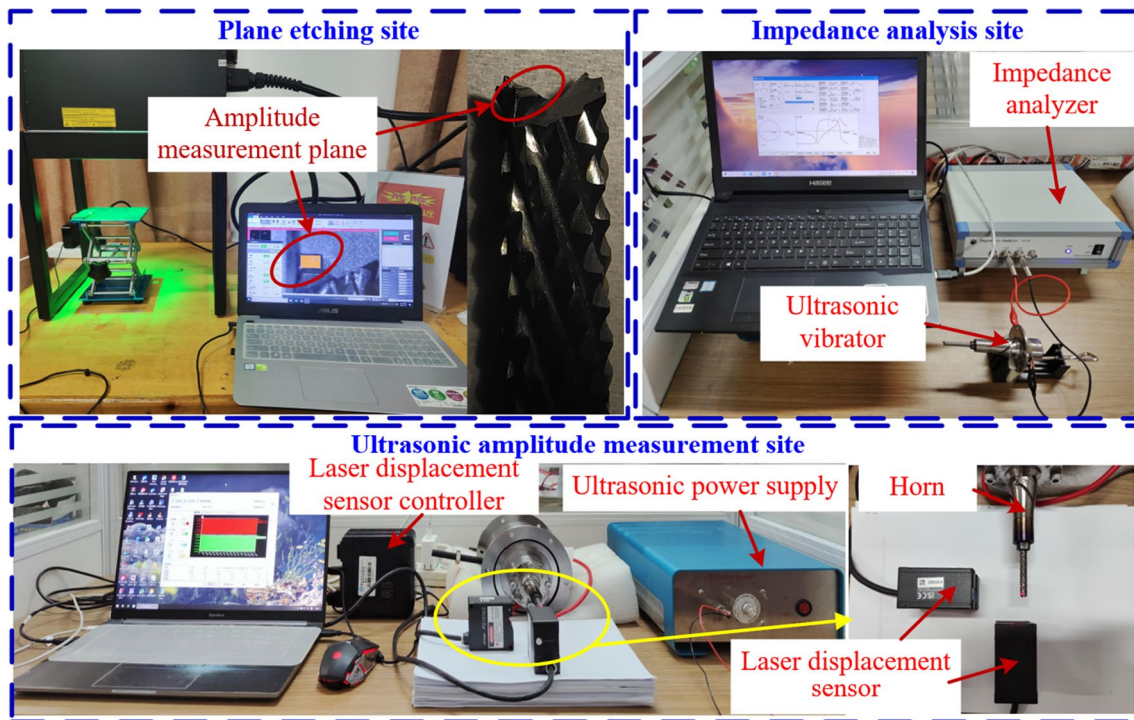**Fig. 6** Low-frequency amplitude and the horn temperature measurement site

Fig. 7 Plane etching, ultrasonic amplitude measurement, impedance testing site

4.2 Experimental details

1. The influence of spindle speed on low-frequency amplitude of the MFVT

Using a single factor test, the machine tool spindle speed is set to 500~2000 rpm. The displacement curves of low-frequency axial vibration are measured at different rotational speeds. The low-frequency vibration performance test was conducted on the VMC850LA CNC machine tool. The performance test of the low-frequency vibration module is carried out in the no-load state of the mixed-frequency vibration tool holder, as reported in Fig. 6.

When the MFVT is tested for low-frequency vibration, the ultrasonic power supply is turned off.

2. The influence of the temperature generated by the self-heating of ultrasonic vibration on the amplitude and resonant frequency of the ultrasonic vibrator

The laser displacement sensor is used to measure the amplitude of the ultrasonic vibrator from the initial moment of operation to 600 s of operation. The FLIR-SC325 infrared thermometer to measure the temperature of the working horn is used, as presented in Fig. 6.

3. The influence of ultrasonic power supply working power on ultrasonic amplitude

Fig. 8 Influence of position error on motion curve of the LFVM
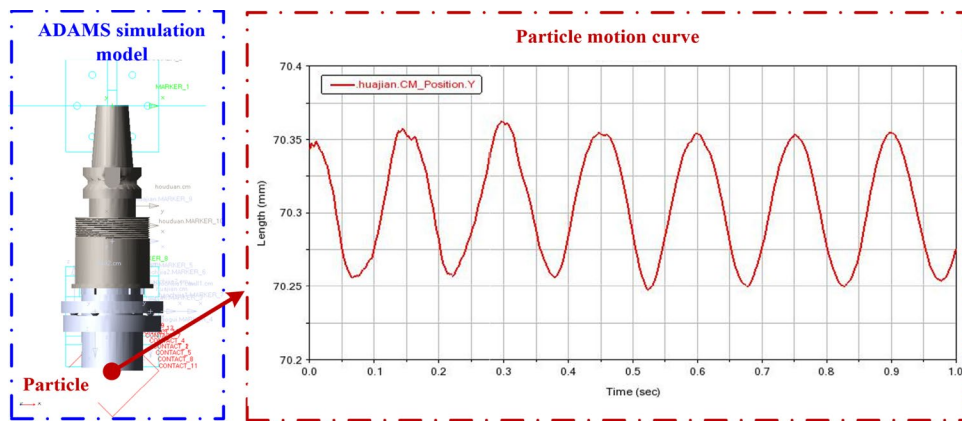
(a) Ideal dynamic simulation model and simulation results
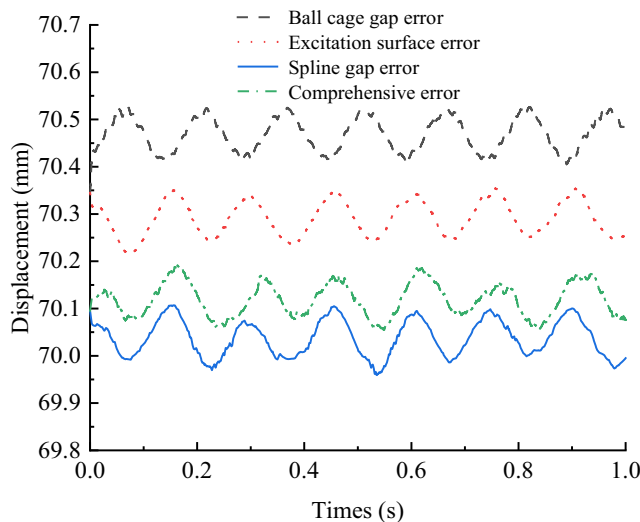
(b) Error dynamics simulation model and simulation results

The impedance analysis of ultrasonic vibrator is carried out by impedance analyzer to verify whether the ultrasonic vibrator meets the design requirements. Using a single-factor test, the operating power of the ultrasonic power supply was set to 25%, 50%, 75%, and 100% of the total power of the power supply. The displacement curve of ultrasonic axial vibration is measured. In the ultrasonic vibration performance test experiment, the laser displacement sensor model KEYENCE LK-H020 was used to measure the amplitude of the ultrasonic vibration module, as shown in Fig. 7. Since the vibration mode of the ultrasonic vibration module is the longitudinal-torsional composite vibration, it includes longitudinal vibration and torsional vibration. Two laser displacement sensors are used to simultaneously measure longitudinal and torsional amplitudes.

The amplitude measurement plane is marked on the edge of the fish scale–milling cutter using the Keyence MD-X2000A laser marking machine. The plane is used for a longitudinal amplitude determination. When measuring the longitudinal

vibration amplitude, the laser beam of the displacement sensor at the plane etched by the tool is aimed. When measuring the torsional amplitude, the laser beam is directed vertically from the side to the side plane of the blade.

5 Discussion

5.1 Vibration performance analysis of the LFVM

5.1.1 Simulation analysis of the LFVM

The simulation 3D model was drawn by SolidWorks and imported into ADAMS dynamic analysis software for dynamic analysis, as shown in Fig. 8a. When the input speed is 100 rpm, the rigid body dynamics simulation of the low-frequency vibration module is conducted. The particle is taken on the spline coupling and the motion curve of the particle is analyzed, as illustrated in Fig. 8a. At the beginning

of the simulation, there are some fluctuations in the motion curve. However, the trend of the waveform and the points with the maximum and minimum values are consistent with the theoretical sine curve. The causes of error are analyzed. During the modeling process, some parts of the assembly are simplified in order to reduce the calculation time of the simulation model. Because of the defects of the modeling software itself, the model cannot achieve the sine curve in the true sense. The physical parameters of the finite element model cannot be completely consistent with the theoretical state.

Based on the analysis of the original position error of the LFVM mentioned above, dynamic simulation models were established respectively for the ball cage gap error, the exciting surface contour error, the spline coupling gap error, and the comprehensive error. The simulation results are presented in Fig. 8. The clearance error and the contour error led to different degrees of deviation in the initial position of the motion curve. The error simulation results of the ball cage are analyzed. The trend of the output motion curve is basically consistent with the theoretical sine curve. However, the movement curve fluctuated. Due to the gap between the ball and the ball cage, the ball pulsates during the operation of the LFVM. Under the action of the spring, the ball collides with the exciting

surface. The collision causes the output motion curve to fluctuate. In the simulation results of the contour error of the excited surface, the output motion curve deviates from the theoretical motion curve. According to the design principle of the LFVM, the shape of the excitation surface directly affects the output displacement curve. Therefore, the contour error of the excitation surface has the greatest influence on the displacement curve. In the simulation results of the gap error of the spline, the wave direction of the output motion curve is consistent with the theoretical motion curve, but the point with the maximum and minimum values is different. The gap between the spline coupling and the guide causes the vibration output part of the LFVM to skew during rotating motion. The deviation direction of spline coupling is random, which will increase the instability of low-frequency vibration. The working speed of the MFVT cannot be a single speed. Therefore, it is necessary to simulate and analyze the working conditions of the MFVT under different speeds. First, the theoretical model was simulated at different speeds, as can be seen from Fig. 9a. When the spindle speed rises from 500 to 2000 rpm, the motion curve of the LFVM is basically consistent with the theoretical sine motion curve. With the increase in rotational speed, the whole motion curve fluctuates periodically. The average amplitude of
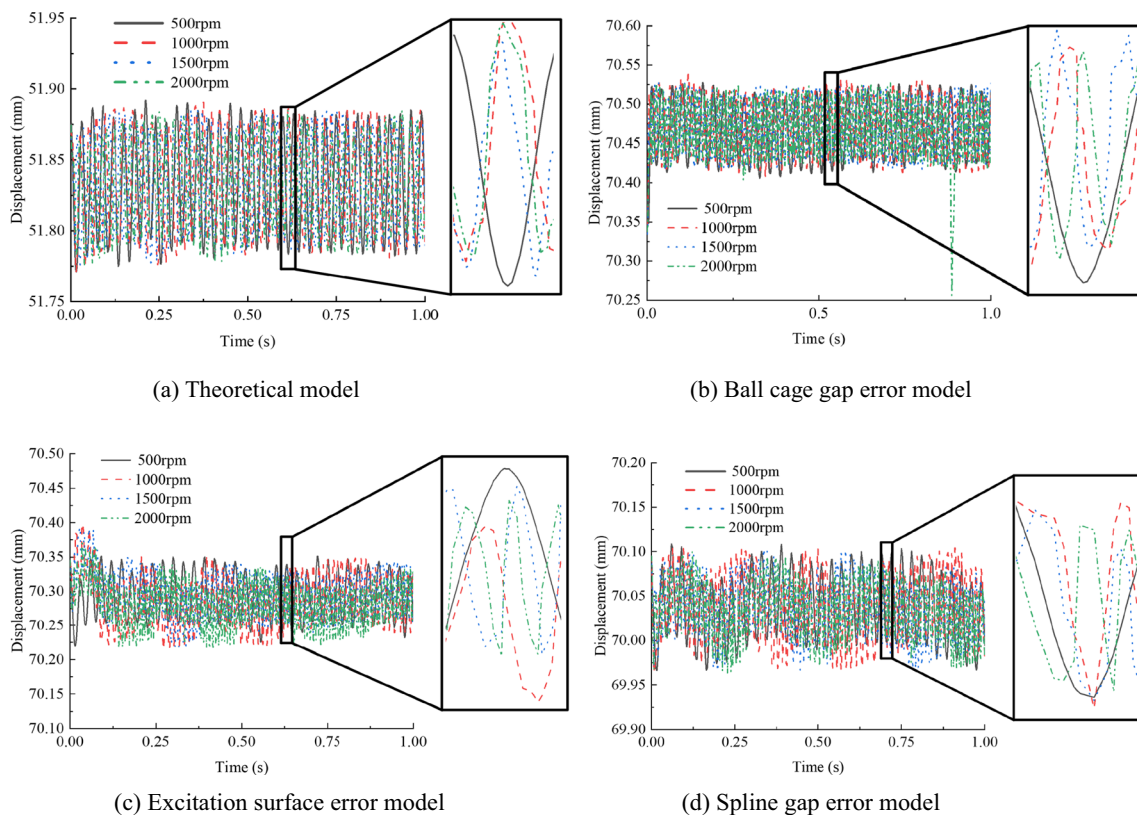

(a) Theoretical model

(b) Ball cage gap error model

(c) Excitation surface error model

(d) Spline gap error model

Fig. 9 The influence of error on the motion curve of the LFVM at different spindle speed

the motion curve decreases to a certain extent, and the simulation results are consistent with the amplitude test results of the LFVM.

In the case of different speeds, the influence of each error on the motion output curve is analyzed. The simulation results of the ball cage gap error model are illustrated in Fig. 9b. The amplitude of the motion curve fluctuates to a certain extent with the increase of the spindle speed, but the motion curve remains sinusoidal. The gap between the ball and the ball cage. The collision between the ball and the ball cage and the exciting surface is aggravated by the increase in rotating speed. When the spindle speed reaches 2000 rpm, there is a big change in the motion curve. The reason for the change is that the exciting surface has a violent collision with the ball. As a component that directly affects the output motion curve of the LFVM, the excitation surface contour plays a role in amplifying its error, as presented in Fig. 9c. With the gradual increase of the speed, the output motion curve appears more serious deviation. The simulation results of the spline coupling clearance error are shown in Fig. 9d. With the increase of the speed, the deviation of the motion curve gradually becomes larger. As the spindle speed increases, the impact between the spline coupling and the tool holder's rear end gradually increases. The impact affects the output of the motion curve of the LFVM, and the actual motion curve deviates from the theoretical motion curve. The influence of the error on the motion output of the LFVM is random and difficult to control.

During the operation of the LFVM, the gap between the two components will cause the impact between the components and affect the output motion curve. The increase in rotational speed will also aggravate the impact, which makes the deviation between the actual motion curve and the theoretical motion curve of the LFVM larger. For the error caused by the contour of the excited surface, the high-processing accuracy

should be selected during processing to reduce the influence of the contour of the surface on the low-frequency vibration output curve. The dimensional accuracy of each component of the LFVM should be selected reasonably to reduce the influence of the clearance error of the moving pair on the motion accuracy.

After determining the relative dimensional accuracy of each part, the total position error of the LFVM is calculated. The total position error is based on the limit size given in the design. The actual processing installation dimensions must be discrete. The maximum position error of the dimensional design can meet the design accuracy, then the reliability of the LFVM can be guaranteed. The LFVM related design dimensions are as follows: The maximum clearance of the spline pair is 0.67 mm, and the maximum clearance between the ball and the ball cage is 0.004 mm. The position error is calculated, as shown in Eq. (30) equation.

$$
\begin{cases}
\Delta h_\Sigma = \Delta h_r + \Delta h_R + \Delta h_\lambda = 0.00906 \ (\text{mm}) \\
\Delta h_r = \Delta r_1 + \Delta r_2 = 0.001 + 0.003 = 0.004 \\
\Delta h_R = \Delta R = 0.005 \\
\Delta h_\lambda = h - h\cos\lambda = 0.00006
\end{cases}
\tag{30}
$$

In summary, the axial error of the mechanism is 0.00906, which can meet the requirements of reliable operation of the mechanism.

5.1.2 Influence of spindle speed on the amplitude of the LFVM

The LFVM is tested and analyzed, as depicted in Fig. 10a, which is the test result of low-frequency vibration when the spindle speed of the machine tool is 100 rpm. The maximum
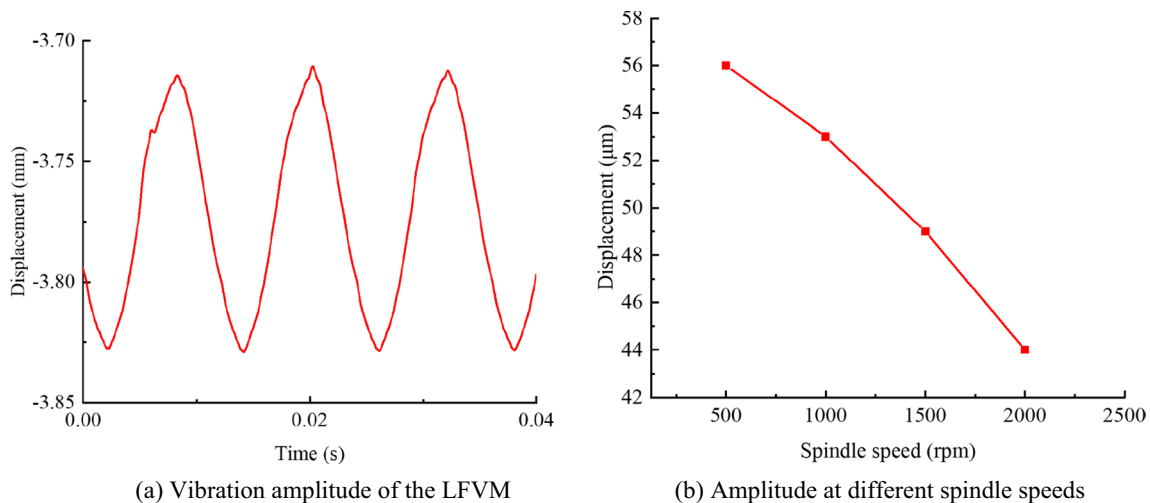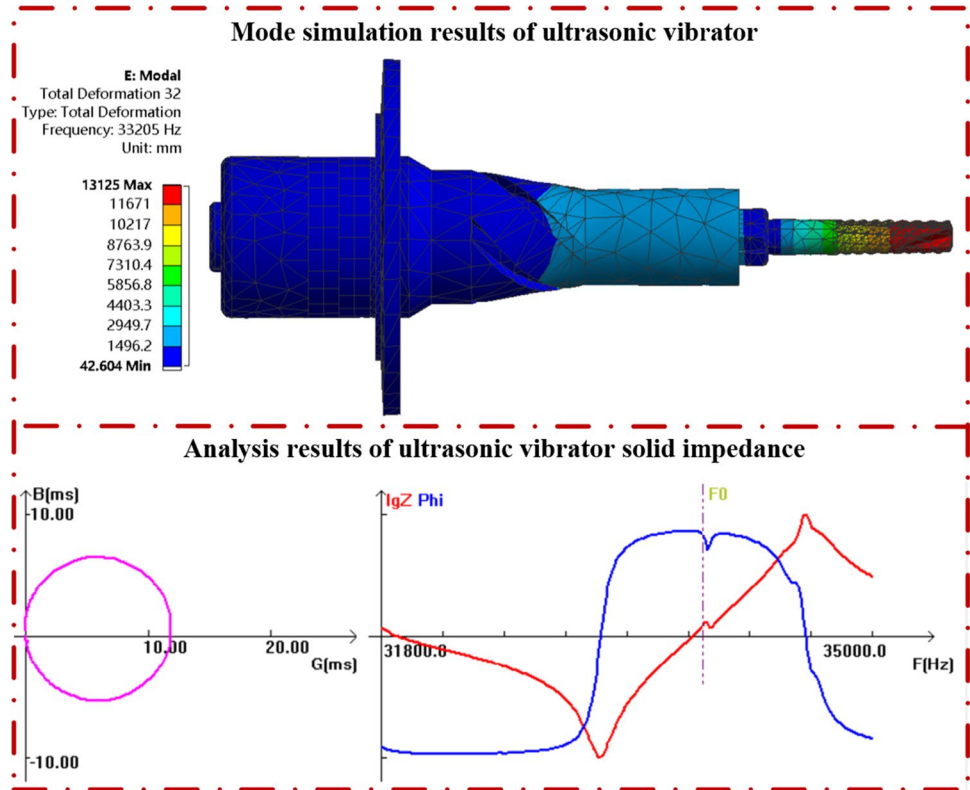

(a) Vibration amplitude of the LFVM

(b) Amplitude at different spindle speeds

Fig. 10 Determination results of the low-frequency vibration amplitude

low-frequency vibration amplitude is 57 μm, which is 3 μm different from the theoretical design value of the low-frequency amplitude, and the low-frequency vibration waveform is consistent with the theoretical design sine waveform.

The amplitude of the mixing vibration tool holder was tested at different machine tool spindle speeds. The test results are illustrated in Fig. 10b. With the increase of spindle speed, the amplitude of the LFVM decreases as a whole. The high spindle speed makes the negative acceleration of the exciting surface gradually increase, and the inertia force during rotation increases with it. When the inertia force of high-speed rotation exceeds the spring elasticity, the spring

recovery is not timely. The excitation surface and the ball will be out of contact. The exciting surface will be separated from the ball briefly, resulting in a certain reduction in the low-frequency vibration amplitude.

5.2 Vibration performance analysis of the UVM

5.2.1 Modal and impedance analysis of UVM

The size parameters of the horn can be obtained from the design theory of the ultrasonic vibrator, which is modeled by SolidWorks. The whole model of the ultrasonic vibrator

Fig. 12 Temperature variation curve of horn during operation
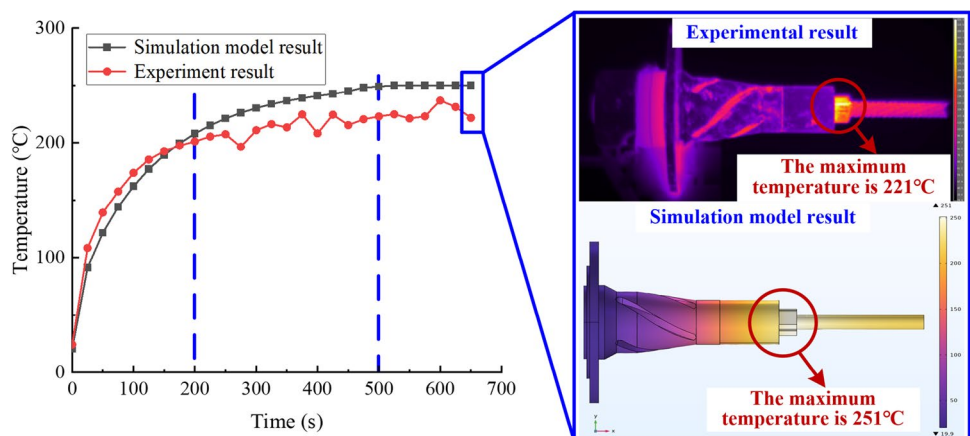
is imported into ANSYS, and the whole modal analysis of the ultrasonic vibrator is carried out.

As reported in Fig. 11, the simulation results of the modal analysis of the ultrasonic vibrator show that the mode of ultrasonic vibration is a longitudinal-torsional compound, and the vibration frequency is 33,205 Hz. The difference between the simulated vibration frequency and the designed theoretical vibration frequency is 205 Hz, which meets the design requirements. Due to the deviation between the performance parameters of the actual material and the theoretical values, errors in processing manufacturing, and assembly are unavoidable. As a result, the theoretical design of the ultrasonic vibrator cannot be consistent with the physical vibration frequency, and the impedance analysis of the ultrasonic vibrator is needed. As can be seen from Fig. 11, the circularity of the admittance circle is good, and no parasitic circle appears. The resonant frequency of the ultrasonic vibrator is 33,011 Hz, which meets the design requirements. Among them, the value of the mechanical quality factor is 423, indicating that the electroacoustic conversion efficiency of the vibrator of the ultrasonic vibration system is high. The dynamic resistance is 0.185, that is, the heat loss of the ultrasonic vibration system is small. In summary, the ultrasonic vibrator meets the design standards and the application requirements.

5.2.2 Temperature variation of the UVM during working process

The overall temperature variation rule of the horn was analyzed, as shown in Fig. 12. The variation trend of the working temperature curve of horn obtained by the simulation model is consistent. When the ultrasonic power supply begins to give excitation voltage, the transducer generates high-frequency vibration. The temperature of the horn increases rapidly when the horn is stimulated by vibration from 0 to 200 s. From 200 to 500 s, the velocity of the temperature rise of the horn gradually slows down. The temperature equilibrium is gradually reached after 500 s. In the temperature equilibrium stage, the maximum temperature of the horn of the simulation model is 251℃, which is 9% different from the maximum equilibrium temperature of the experimental results.

From the simulation analysis, it can be seen that the greatest impact on the temperature of the horn is the energy loss at the contact position between the collet and the tool. As can be seen from Fig. 12, the maximum temperature of the horn is located at the end of the collet (that is, the position where the collet contacts the tool). The experimental results are consistent with the simulation results. Its overall temperature change curve is similar to the temperature change law of vibration self-heating simulation. The analysis reasons are as follows. The materials of the horn, collet, and tool are different. The damping of different materials is different, that is, the isotropic internal loss factor is different. Among them, the isotropic internal loss factor of spring steel is 0.00005. The horn and tool collet are connected by bolts, which can be equivalent to equivalent viscous damping, and its damping is 0.05. Mechanical vibration waves will cause losses when they are transmitted through different materials, and this loss will be converted into the heat energy of the components. The connection between the tool and the collet results in a gap between the two. Mechanical vibration waves are reflected and refracted in these gaps, resulting in energy loss and heat energy.

The results of vibration self-heating simulation and experiments prove that the temperature of the horn will eventually reach thermal equilibrium, as reported in Fig. 12. The reason for reaching thermal equilibrium is as follows.
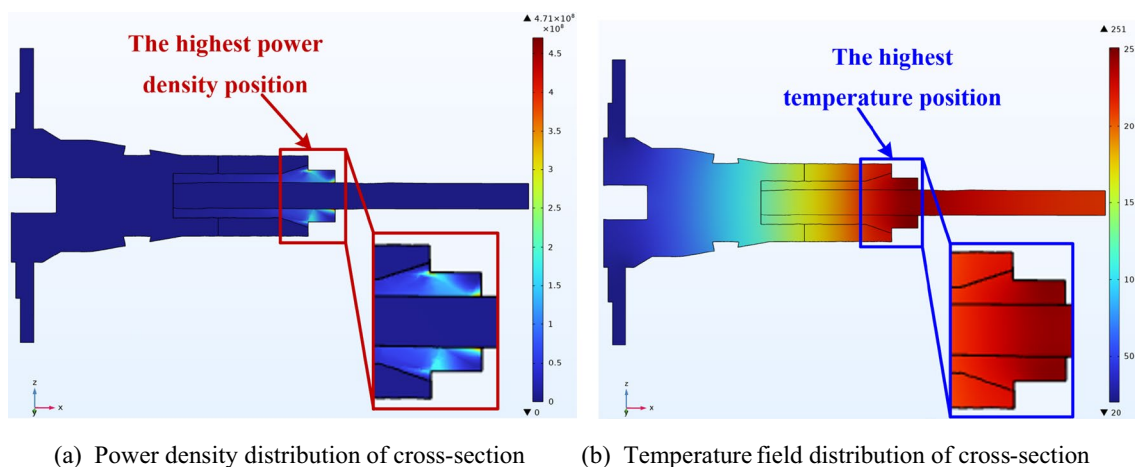

(a) Power density distribution of cross-section   (b) Temperature field distribution of cross-section

Fig. 13 Temperature field and power density distribution of the horn section

(a) Longitudinal amplitude

(b) Torsional amplitude

(c) Amplitude under different power states
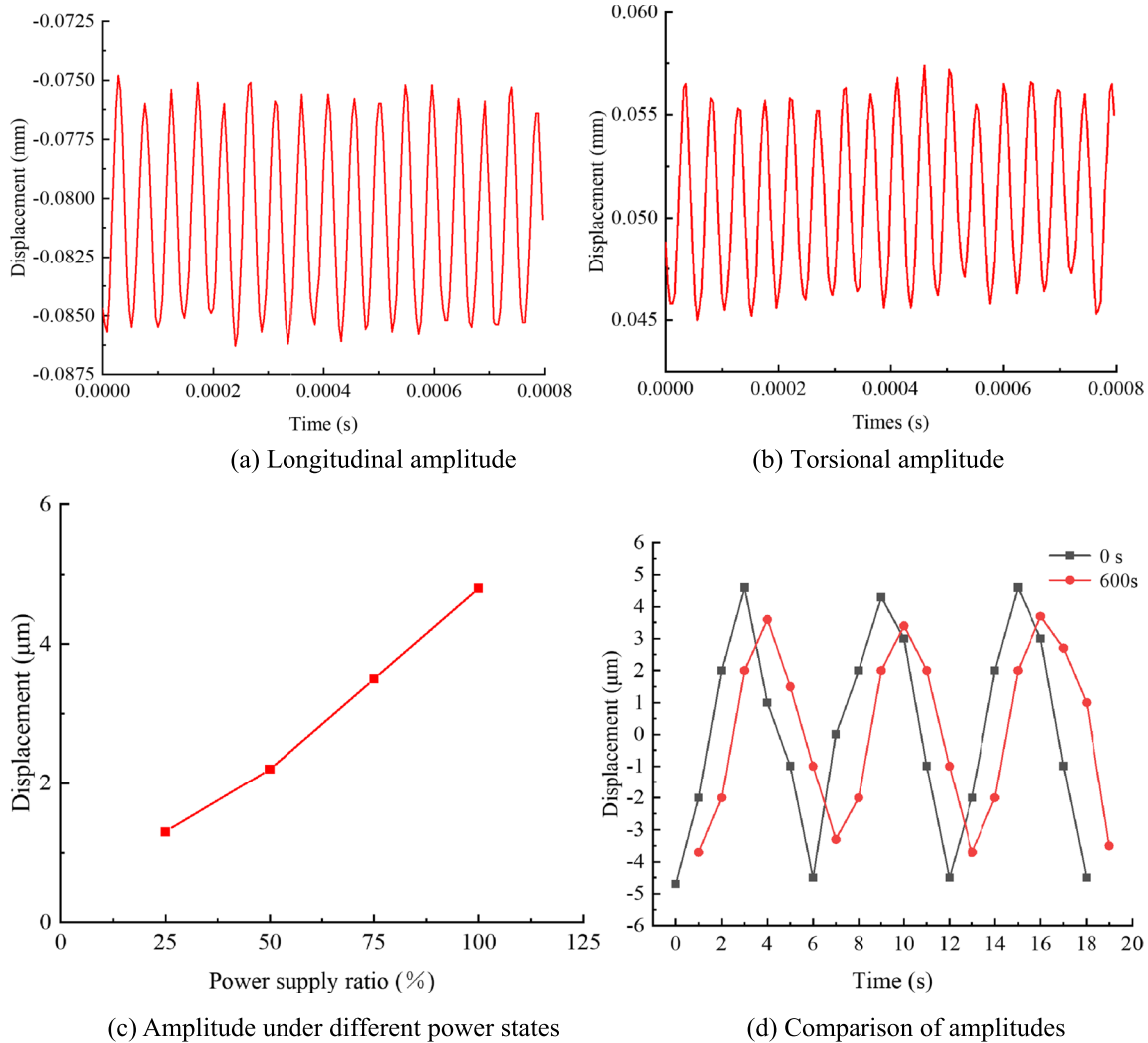
(d) Comparison of amplitudes

Fig. 14 Ultrasonic amplitude measurement results

When the temperature rises, the speed at which the horn exchanges heat with the outside world increases. As the temperature of the horn increases, the amplitude will decrease and the resonant frequency will decrease. As a result, the energy loss of the horn caused by mechanical vibration is reduced. Therefore, under the combined effect of these two aspects, the temperature of the horn will gradually reach thermal equilibrium after a certain period of time.

In order to understand the thermal energy generation mechanism of the horn, the temperature variation of the horn during operation is simulated and analyzed. The total power density distribution of the horn cross-section is shown in Fig. 13a. The total power density peaks at the position where the collet contacts the tool, reaching $4.65 \times 107 W/m^3$. During the working process of the ultrasonic vibrator, a lot of heat is generated at the end of the collet, and the heat is transferred to the rest of the ultrasonic vibrator. At high-frequency vibration, the mechanical loss caused by the

damping of the horn material is small, and the influence on the overall temperature change of the ultrasonic vibrator is small. The peak temperature occurs at the position where the collet contacts the tool, and the temperature at this position is 251℃. As can be seen from Fig. 13b, the small temperature change at the back end of the horn is conducive to maintaining a good energy conversion rate of the ultrasonic vibrator in operation.

5.2.3 Influence of temperature on the resonant frequency of the UVM

The UVM is tested and analyzed, and the amplitude is measured when the ultrasonic vibration module is running stably. The measurement are taken multiple times, and the results are averaged. The longitudinal vibration amplitude measurement results are shown in Fig. 14a, and the torsional amplitude measurement results are illustrated in Fig. 14b. The

longitudinal amplitude is 4.8 μm and the torsional amplitude is 4.1 μm, which meets the design requirements.

In ultrasonic vibration–assisted processing, the amplitude plays a decisive role in cutting processing. When processing different materials, corresponding and reasonable amplitudes need to be selected. Therefore, the amplitude of the ultrasonic power supply under different power states was tested. The test results are depicted in Fig. 14c. The amplitude increases with increasing power supply. As the power supply increases, the acoustic-electrical effect increases, and the amplitude of ultrasonic vibration increases. The laser displacement sensor was used to measure the amplitude at the initial moment and at 600 s of vibration.

The output of ultrasonic longitudinal vibration and ultrasonic torsional vibration should be considered comprehensively in the actual processing. Based on the principle of acoustic refraction, the UVM converts longitudinal ultrasonic vibration into longitudinal and torsional combined vibration. The amplitude of longitudinal ultrasonic vibration is easy to measure. Therefore, the influence of temperature on the vibration performance of the UVM was studied by measuring the longitudinal ultrasonic vibration amplitude of the UVM. As can be seen from Fig. 14d, the test results show that the amplitude dropped from 4.7 to 3.4 μm. The amplitude after vibration heating is smaller than the initial amplitude. As the temperature increases, the resonant frequency of the horn continues to decrease. The excitation frequency of 33,000 Hz at the big end of the horn will continuously deviate from the resonant frequency of the horn. The amplitude is the largest under resonance. After the resonant frequency of the horn continues to deviate from the resonant frequency, the amplitude will decrease.

For the ultrasonic vibrator, its temperature increases gradually with the increase of working time. Assuming that the temperature of the horn is uniformly distributed, the formula of its longitudinal resonance frequency is as follows:

$$f = \frac{1}{2L_0(1+\alpha\Delta T)}\sqrt{\frac{E_0(1-\beta\Delta T)}{\rho_0/(1+\pi r_i^2\alpha\Delta T)}} \tag{31}$$

where L_0 is the initial length of the horn, α is the coefficient of thermal expansion, E_0 is the elastic modulus of horn material, ρ_0 is the initial density, and r_i is the radius of the structure of each part of the ultrasonic vibrator.

As can be seen from Eq. (42), the frequency drift is negatively correlated with temperature rise. With the increase in temperature, the frequency drift of the horn will increase continuously. As the temperature of the material increases, the elastic modulus decreases, and the coefficient of thermal expansion increases. With the increase of the thermal expansion coefficient, the structural length of the horn increases and the density decreases. The change of thermal expansion

coefficient and elastic modulus of 45 steel with temperature, as can be seen from Table 4. The corresponding parameters are substituted into Eq. (40) for calculation. The results show that the resonant frequency of ultrasonic vibrator shifts with the change of material properties. The resonant frequency will decrease with the increase in temperature. When $T = 251℃$, the resonant frequency becomes 32,641 Hz.

6 Conclusion

Based on the advantages of ultrasonic vibration and low-frequency vibration, the combination of high-frequency and low-frequency vibration–assisted processing devices are proposed. The simulation and experimental study of the MFVT are carried out. Then, the main conclusions are as follows:

(1) Based on the kinematic model of high- or low-frequency complex vibration, the overall design scheme of MFVT is determined and the design theory of MFVT is derived. The performance of LFVM and UVM is verified by testing, and the design requirements are met.

(2) The transmission accuracy of LFVM is verified by calculating the position error, and the contour error of the exciting surface has the greatest influence on the output curve. With the increase of the speed, the deviation of the motion curve will be greater. The low-frequency vibration amplitude decreases with the increase of tool holder speed.

(3) The heat generated at the end of the tool chuck of the ultrasonic vibration module is the main heat source of the ultrasonic vibrator. Both the amplitude and resonant frequency of the ultrasonic vibrator decay with the increase of temperature. The material used for making ultrasonic vibrators should have the characteristics of low damping, high strength, and strong thermal stability. The bolt material at the joint shall be consistent with that of the horn.

Declarations

Ethics approval Not applicable.

Consent to participate Not applicable.

Consent for publication Not applicable.

Competing interests The authors declare no competing interests.

References

1. Bhaskar NN, Venkatesh MK (2024) Investigation of the mechanical performance of carbon fiber reinforced polymer and aluminum 2024 alloy lap joints[J]. J Inst Eng (India): Series D 2024:1–11
2. Nurazzi NM, Asyraf MRM, Khalina A, Abdullah N, Aisyah HA, Rafiqah SA, Sabaruddin FA, Kamarudin SH, Norrrahim MNF, Ilyas RA, Sapuan SM (2021) A review on natural fiber reinforced polymer composite for bullet proof and ballistic applications. Polymers 13(4):646
3. Hegde S, Shenoy BS, Chethan KN (2019) Review on carbon fiber reinforced polymer (CFRP) and their mechanical performance. Mater Today: Proc 19:658–662
4. Panchagnula KK, Palaniyandi K (2018) Drilling on fiber reinforced polymer/nanopolymer composite laminates: a review. J Market Res 7(2):180–189
5. Lee PA, Kim Y, Kim BH (2015) Effect of low frequency vibrationon micro EDM drilling. Int J Precis Eng Manuf 16:2617–2622
6. Seeholzer L, Voss R, Marchetti L, Wegener K (2019) Experimental study: comparison of conventional and low-frequency vibration-assisted drilling (LF-VAD) of CFRP/aluminium stacks. Int J Adv Manuf Technol 104:433–449
7. Pecat O, Brinksmeier E (2014) Tool wear analyses in low frequency vibration assisted drilling of CFRP/Ti6Al4V stack material. Procedia Cirp 14:142–147
8. Sadek A, Attia MH, Meshreki M, Shi B (2013) Characterization and optimization of vibration-assisted drilling of fibre reinforced epoxy laminates. CIRP Ann 62(1):91–94
9. Lu Y, Yuan S, Chen Y (2019) A cutting force model based on kinematic analysis in longitudinal and torsional ultrasonic vibration drilling. Int J Adv Manuf Technol 104:631–643
10. Xu J, Feng P, Feng F, Zha H, Liang G (2021) Subsurface damage and burr improvements of aramid fiber reinforced plastics by using longitudinal–torsional ultrasonic vibration milling. J Mater Process Technol 297:117265
11. Cong WL, Pei ZJ, Treadwell C (2014) Preliminary study on rotary ultrasonic machining of CFRP/Ti stacks. Ultrasonics 54(6):1594–1602
12. Cong WL, Pei ZJ, Deines TW, Liu DF, Treadwell C (2013) Rotary ultrasonic machining of CFRP/Ti stacks using variable feedrate. Compos B Eng 52:303–310
13. Zhang SJ, Jiao F, Li YX, Wang D, Niu Y (2020) Experimental study on high and low frequency compound vibration drilling of carbon fiber reinforced plastic/titanium alloy laminated structure. Mach Design Res 36(06):120–124
14. Ma QY, Ma QH, Wang B, Yu DG (2013) Mechanical axial vibration system design for deep holes drilling. Mach Design Res 4:86–87+92
15. Wu SS, Lin XM, Lu ZW (2013) Measuring method for the signal distortion of axial thrust and mechanical vibration platform. Appl Mech Mater 397:1685–1690
16. Laporte S, De Castelbajac C (2013) Major breakthrough in multi material drilling, using low frequency axial vibration assistance. SAE Int J Mater Manuf 6(1):11–18
17. Jiao F, Li Y, Wang D, Tong J, Niu Y (2021) Development of a low-frequency vibration-assisted drilling device for difficult-to-cut materials. Int J Adv Manuf Technol 116:3517–3534
18. Liu Z, Liu H, Zhao D, Wang C, Wang T (2020) Design and finite element analysis of axial low-frequency vibration tool-holder. In Journal of Physics: Conference Series (Vol. 1653, No. 1, p. 012040). IOP Publishing
19 Shamoto E (2014) Vibration cutting-fundamentals and application. J Japan Soc Precision Eng 80(5):457–460
20. Xu LH, Na HB, Han GC (2018) Machinablity improvement with ultrasonic vibration–assisted micro-milling. Adv Mech Eng 10(12):1687814018812531
21. Harkness P, Cardoni A, Lucas M (2009) Ultrasonic rock drilling devices using longitudinal-torsional compound vibration. In 2009 IEEE International Ultrasonics Symposium (pp. 2088–2091). IEEE
22. Al-Budairi H, Lucas M, Harkness P (2013) A design approach for longitudinal–torsional ultrasonic transducers. Sens Actuators, A 198:99–106
23. Tsujino J, Ueoka T, Otoda K, Fujimi A (2000) One-dimensional longitudinal–torsional vibration converter with multiple diagonally slitted parts. Ultrasonics 38(1–8):72–76
24. Nath C, Rahman M, Neo KS (2009) A study on ultrasonic elliptical vibration cutting of tungsten carbide. J Mater Process Technol 209(9):4459–4464
25. Kim GD, Loh BG (2007) An ultrasonic elliptical vibration cutting device for micro V-groove machining: kinematical analysis and micro V-groove machining characteristics. J Mater Process Technol 190(1–3):181–188
26. Ishikawa KI, Suwabe H, Nishide T, Uneda M (1998) A study on combined vibration drilling by ultrasonic and low-frequency vibrations for hard and brittle materials. Precis Eng 22(4):196–205
27. Meng QRG, Hou SJ, Li K, Qu YX, Chen T (2020) Investigation on ultrasonic and low-frequency rotating vibration drilling. J Vib Meas Diagn 1004–6801.2020.02.012
28. Li YX (2020) Development and experimental study of high and low frequency compound vibration drilling device for precise and efficient drillingof CFRP / titanium alloy laminated structure. HeNan Polytechnic unicersity
29. Moens D, Vandepitte D (2007) Interval sensitivity theory and its application to frequency response envelope analysis of uncertain structures. Comput Methods Appl Mech Eng 196(21–24):2486–2496
30. Rothbart HA, Klipp DL (2004) Cam design handbook. J Mech Des 126(2):375–375